Laves Intermetallics in Stainless Steel-Zirconium Alloys*

Daniel P. Abraham and Sean M. McDeavitt
Argonne National Laboratory
Chemical Technology Division
9700 S. Cass Avenue
Argonne, IL 60439
Phone: (630) 252-4332
Fax: (630) 252-5246

James W. Richardson, Jr.
Intense Pulsed Neutron Source Division
Argonne National Laboratory
Chemical Technology Division
9700 S. Cass Avenue
Argonne, IL 60439
Phone: (620) 252-3554
Fax: (630) 252-4163

To be presented at 4th International Conference on
High-Temperature Intermetallics
San Diego, CA
April 27 through May 1, 1997

*Work supported by the U.S. Department of Energy, Nuclear Energy Research and Development Program, under Contract No. W-31-109-Eng. 38.

Laves Intermetallics in Stainless Steel-Zirconium Alloys

Daniel P. Abraham, James W. Richardson Jr.*, Sean M. McDeavitt

Chemical Technology Division and * Intense Pulsed Neutron Source Division

Argonne National Laboratory, 9700 S. Cass Avenue, Argonne, IL 60439

Abstract

Laves intermetallics have a significant effect on properties of metal waste forms being developed at Argonne National Laboratory. These waste forms are stainless steel-zirconium alloys that will contain radioactive metal isotopes isolated from spent nuclear fuel by electrometallurgical treatment. The baseline waste form composition for stainless steel-clad fuels is stainless steel-15 wt.% zirconium (SS-15Zr). This article presents results of neutron diffraction measurements, heat-treatment studies and mechanical testing on SS-15Zr alloys. The Laves intermetallics in these alloys, labeled $Zr(Fe,Cr,Ni)_{2+x}$, have both C36 and C15 crystal structures. A fraction of these intermetallics transform into $(Fe,Cr,Ni)_{23}Zr_6$ during high-temperature annealing; we have proposed a mechanism for this transformation. The SS-15Zr alloys show virtually no elongation in uniaxial tension, but exhibit good strength and ductility in compression tests. This article also presents neutron diffraction and microstructural data for a stainless steel-42 wt.% zirconium (SS-42Zr) alloy.

Introduction

Laves phases, compounds with the general formula AB_2, have one of the following crystal structures: C14 (hexagonal, $MgZn_2$-type), C15 (cubic, $MgCu_2$-type) and C36 (dihexagonal, $MgNi_2$-type) [1-3]. The abundance of these phases among intermetallic compounds has been attributed to geometric factors governing the ordered arrangement of atoms on lattice sites. Space filling in binary compounds is most efficient when atoms exhibit the ratio $d_A/d_B = \sqrt{3}/\sqrt{2} \approx 1.225$, where d is the diameter of the spherical atoms [1]. Laves phases occur for atomic diameter ratios between ~ 1.05 and 1.68. The hexagonal polytypes, C14 and C36, are more abundant

for atom size ratios closer to 1.225, whereas the C15 polytype is more frequent for ratios above 1.225 [4]. The occurrence of individual Laves polytypes has also been related to electron concentrations (valence electron per atom) in the compound [1, 5]

Laves intermetallics are prominent in stainless steel-zirconium (SS-Zr) alloys being developed as metal waste forms for the electrometallurgical treatment of spent nuclear fuel [6]. In this process, uranium is separated out of chopped fuel pins in a molten salt electrolyte [7]. The metallic remnants in the anode baskets of the electrorefiner, which include fuel cladding hulls, noble metal fission products and small amounts of other metals, constitute the metal waste form. These metal wastes will be stabilized by melting and casting into uniform, corrosion-resistant alloys for eventual disposal in a geologic repository. Two baseline waste form compositions are being developed: (1) stainless steel-15 wt.% zirconium (SS-15Zr) for stainless steel-clad fuels and (2) zirconium-8 wt.% stainless steel (Zr-8SS) for Zircaloy-clad fuels. The cladding hulls are used as a major alloying component to minimize the addition of external alloying elements to the metal waste forms.

Abraham et al. [6] had previously presented the microstructures in type 304 stainless steel - zirconium alloys containing from 5 to 92 wt.% zirconium; a $ZrFe_2$-type Laves intermetallic, $Zr(Fe,Cr,Ni)_{2+x}$, was observed in all alloys studied. In SS-15Zr alloys, $Zr(Fe,Cr,Ni)_{2+x}$ constitutes ~50% of the microstructure and has a significant effect on waste form properties [8]. An understanding of this intermetallic is hence crucial to predicting SS-15Zr alloy behavior during processing and long-term storage. This article extends our understanding of $Zr(Fe,Cr,Ni)_{2+x}$ by presenting neutron diffraction measurements on SS-15Zr alloy phases. Neutron diffraction data are also reported for a stainless steel-42 wt.% zirconium (SS-42Zr) alloy; this composition was expected to yield a single-phase Laves intermetallic. Mechanical testing results and effects of heat treatment on $Zr(Fe,Cr,Ni)_{2+x}$ stability are also discussed.

Alloy Preparation

Ingots of SS-15Zr alloy weighing ~ 3 kg were produced in an induction casting furnace attached to a controlled-atmosphere glovebox. Type 316 stainless steel and zirconium metal rods were charged into 10-cm (4-in.) diameter yttrium oxide crucibles and alloyed at 1600°C under high purity argon for ~ 1 h. Alloy ingots were

made by cooling the melt within the crucible; the yttrium oxide crucibles fractured during the solidification process allowing easy removal of the ingots. Examination of ingot surfaces revealed a ~ 1 μm melt-crucible interaction layer, which was easily removed by surface grinding. Specimens for neutron diffraction, scanning electron microscope (SEM) examination and mechanical testing were subsequently prepared by sectioning and machining operations.

Ingots of SS-42Zr alloy each weighing ~ 25 g were produced in a tungsten-element furnace using 316 stainless steel and high purity zirconium. The starting materials were placed in yttrium oxide crucibles and melted at 1650°C in an argon atmosphere for 2 h. Details of the experimental arrangement for ingots produced by this technique have been provided elsewhere [6]. The SS-42Zr alloys were brittle and difficult to section; specimens for compression testing were produced by wire cutting the alloy. Neutron diffraction specimens were prepared by crushing the ingot using a mortar and pestle.

Experimental Procedure and Results

A. Chemical Analysis

Alloy compositions and homogeneity were confirmed by chemical analysis on specimens from various sections of the ingot. Typical compositions of SS-15Zr and SS-42Zr alloys in weight percent are listed in Table 1. It is evident that iron, chromium, nickel, and zirconium are the major elements in both alloys. Minor elements such as Mn, Mo and Si are not expected to have a significant impact on alloy properties.

B. Phase Identification

The crystal structure of phases was revealed by neutron diffraction. Time-of-flight (TOF) neutron powder diffraction data were collected on the General Purpose Powder Diffractometer (GPPD) [9] at the Intense Pulsed Neutron Source (IPNS) of Argonne National Laboratory (ANL). TOF experiments are carried out at a fixed scattering angle, and diffraction patterns are generated as a function of incident neutron wavelength, which is proportional to d-spacing. Rietveld refinements [10] were carried out using data from six separate detector banks,

each one positioned at a fixed 2Θ angle relative to the incident beam. Each detector bank accesses a limited range of d-spacings, depending upon the range of wavelengths available. Ranges for the banks used in this study are 2Θ = 148 , d ~0.5-3.0 Å; 90 , 0.7-4.0 Å; and 60 , 0.8-5.4 Å. For many applications, such as those without reflections with d-spacings higher than 3.0 Å, refinement of backscattering data (2Θ= 148) only is sufficient. Combined analysis of the six data banks was chosen here for three reasons: (1) Slight variations in refined lattice parameters for the different banks are used to calculate minor corrections ($\Delta a/a \lceil 2x10^{-4}$) caused by shifts in the centroid of scattering from the high scattering cross section of these materials. (2) Each detector bank views the sample from a different orientation, so we obtained an assessment of preferred orientation (texture) from variations in intensity from bank to bank. (3) Calculated phase fractions can be obtained by averaging the results from all banks, reducing the influence of texture.

All phases identified by neutron diffraction in SS-15Zr and SS-42Zr alloys are presented with lattice parameters and phase fractions (expressed as volume percent) in Table 2. Lattice parameters and phases in an iron-15 wt.% zirconium (Fe-15Zr) and an iron-10 wt.% chromium-45 wt.% zirconium (Fe-10Cr-45Zr) alloy are also listed in Table 2 for comparison [11, 12].

Five phases were identified in SS-15Zr alloys: ferrite (α-SS), austenite (γ-SS), $(Fe,Cr,Ni)_{23}Zr_6$, and the $Zr(Fe,Cr,Ni)_{2+x}$ Laves polytypes C36 and C15. The presence of Laves C14 could not be determined conclusively because it is difficult to distinguish from C36; both structures are hexagonal, with nearly identical basal plane dimensions. The axial dimension of the C36 structure is, however, double that of C14; so the diffraction pattern of C36 is the same as the C14 pattern but with extra lines [5]. The Laves C14 phase may be present in very small amounts with lattice parameters a = 0.4909 nm and c = 0.8008 nm.

The lattice parameters of phases in SS-15Zr alloys were not altered by heat treatment for 2 h at 1275°C; however, the volume percent of various phases was altered (see Table 2). The amount of $(Fe,Cr,Ni)_{23}Zr_6$, is 11% in the annealed alloy, more than five times its content in the as-cast alloy. The austenite content decreased to 4% from 9% in the as-cast alloy, while the Laves C15 content decreased to 13% from 16% in the as-cast alloy.

Although the SS-42Zr composition, by analogy with the Fe-Zr phase diagram [13], was expected to yield a single-phase Laves intermetallic, two sets of diffraction peaks (one strong, one weak) were observed in this

alloy; both sets correspond to distinct C14 phases as noted in Table 2. A C14 Laves phase was also the dominant feature in the ternary Fe-10Cr-45Zr alloy. Three phases, α-Fe, $Fe_{23}Zr_6$, and a C36-type $ZrFe_2$ phase were identified in the Fe-15Zr diffraction pattern: Laves C15, observed by electron diffraction [14], may also be present in this alloy. The C15 lattice parameter in Table 2 is from the work of Bruckner et al. who studied the effect of concentration variations on the $ZrFe_2$ lattice [15].

C. Microstructural Analysis

The SEM examination of alloy specimens was performed with a JEOL 6400 scanning electron microscope. Standardless quantitative analysis of individual phases was obtained with an EDS spectrometer and Voyager II software from NORAN instruments. The uncertainty in elemental compositions determined by this method is 3% of the measured value.

A typical microstructure of as-cast SS-15Zr alloy, shown in Fig. 1, contains a mixture of coarse and fine eutectics. The dark regions are α-SS, while the bright regions are the $Zr(Fe,Cr,Ni)_{2+x}$ phase. Austenite (γ-SS) and $(Fe,Cr,Ni)_{23}Zr_6$ were also occasionally observed in the microstructure. Elemental compositions of the phases are shown in Table 2. The $Zr(Fe,Cr,Ni)_{2+x}$ phase contained only 24 at.% Zr, a substoichiometry of more than 25% from the expected 33.3 at.% Zr. Since we were unable to distinguish between the various Laves polytypes under the SEM, the Laves intermetallic composition has been arbitrarily assigned to the C36 structure. The C15 polytype (and C14, if present) may have similar elemental compositions.

The SS-15Zr alloys that had been annealed for 2-4 h at temperatures from 1000-1300°C contained larger amounts of the $(Fe,Cr,Ni)_{23}Zr_6$ phase. The "gray" regions in Figs. 2a and 2b correspond to $(Fe,Cr,Ni)_{23}Zr_6$ in an alloy annealed for 2 h at 1275°C. The phase contained ~ 20 at.% Zr, which is its expected zirconium content at stoichiometry. Bright and dark areas were often seen within $(Fe,Cr,Ni)_{23}Zr_6$; they are seen clearly in Fig. 2b. The dark areas were α-SS; the bright areas were mainly zirconium (95-98 at.%) and will be referred to as α-Zr. These zirconium-rich regions were not observed outside the gray phase, indicating their association with $(Fe,Cr,Ni)_{23}Zr_6$ formation. Peaks corresponding to α-Zr were not observed in diffraction patterns; the volume fraction of this phase may have been too small to produce diffraction peaks.

A single-phase microstructure was typical of the SS-42Zr alloy. However, regions, such as shown in Fig. 3, were occasionally observed. The dominant (matrix) phase in Fig. 3 contains ~31 at.% Zr and corresponds to the set of strong C14 Laves intermetallic peaks observed in the diffraction pattern. This phase shows only slight zirconium substoichiometry and is identified as Laves C14-1 in Table 2. The "triangular gray" phase in Fig. 3 corresponds to the set of weak C14 peaks observed in the diffraction pattern. This phase has an elevated nickel content (~24 at.% Ni), shows > 25% zirconium sub-stoichiometry, and is identified as Laves C14-2. In addition to the Laves intermetallics, a phase with <0.1 at.% Zr is shown in Table 2 and marked by arrows in Fig. 3. This phase is labeled sigma because its iron and chromium content are those expected for the σ-phase observed in Fe-Cr alloys [16]. Sigma phase peaks were not observed in the diffraction pattern, probably because of its very small content in the alloy.

D. Mechanical Testing

Uniaxial tensile and compression tests on SS-15Zr alloys were performed at Westmoreland Research and Testing, Inc., Johnstown, PA according to ASTM standards E8-96 and E9-89, respectively. The tensile test was performed on round-`bar specimens with a gage length of 2.54 cm (1 in.) and 0.635 cm (0.25 in.) reduced section diameter. Cylindrical specimens, 1.27 cm (1/2 in.) dia. and 2.54 cm (1 in.) long, were used for compression tests. Microhardness was measured with a Buehler Micromet 2003 microhardness tester.

For the uniaxial tensile test, SS-15Zr alloy specimens were loaded at a rate of 2.2×10^{-4} cm/s. The tensile modulus of elasticity was calculated to be 180 20 GPa (26 3 Msi), which is similar to the values reported for stainless steels [16]. The specimens failed at a tensile stress of 262 28 MPa (38 4 ksi) and showed virtually no elongation. This failure stress is similar to the typical yield stress of 316 stainless steel [16]. SEM examination of the tensile fracture surface showed that the dominant fracture process was brittle cleavage; ductile fracture processes such as microvoid coalescence were not observed. The fracture surface, shown in Fig. 4, resembles the eutectic structure in Fig. 1. The failure appears to have been caused by the inability of the intermetallic to deform during the yielding of the stainless steel phases.

Alloy specimens tested in compression were also loaded at a rate of 2.2×10^{-4} cm/s. Initial strain values, up to 2%, were measured with a high-precision extensometer mounted on the specimen. Strain values beyond 2% were calculated from the crosshead displacement. The yield strength of specimens, calculated at 0.2% offset, ranged from 667 to 688 MPa (96.7 to 99.7 ksi), while the compressive strength ranged from 1131 to 1151 MPa (164 to 167 ksi). The alloys showed from 6.9 to 8.1% strain before fracturing into two pieces. A typical stress-strain curve in compression is shown in Fig. 5. The modulus in compression and Poisson's ratio of the alloy were also measured; these values are 180 7 GPa (26 1 Msi) and 0.3, respectively.

Compression testing was performed on a single cube-shaped SS-42Zr specimen. The cube cross-section was 0.62 x 0.62 = 0.384 sq. cm. (0.06 sq.in.). The specimen showed no elongation and failed at a compressive stress of 131 MPa (19 ksi). Liu et al. reported yield stress of 730 MPa and compression strains of 46 to 48% for the Fe_2Zr intermetallic in an Fe-15Zr alloy [14]. The low elongation values and compression strains may be due to the presence of defects in the SS-42Zr specimen.

Microhardness measurements were made using a 1000-g load and a 10-s loading time. In SS-15Zr, the phase dimensions were small enough that the indenter impressed both the Laves and the stainless steel phases in the eutectic. The microhardness measured averaged 380 HK (~370 HV) for the as-cast SS-15Zr alloy, which is almost twice that of 316 stainless steel. Fine cracks were observed in the intermetallic phase within the eutectics. The average microhardness in the SS-42Zr alloy was 750 HK (~720 HV); cracking was seen at indentation corners. The hardness of the Laves intermetallic is thus roughly twice that of the eutectic in as-cast SS-15Zr alloy and more than three times that of 316 stainless steel.

Discussion

A. Phases in the Microstructure

Type 316 is an austenitic stainless steel; however, Table 2 shows that the predominant stainless steel phase in SS-15Zr alloys is α-SS, not γ-SS. Table 2 also shows that very little zirconium is present in both α-SS and γ-SS. Zirconium combines with iron, chromium, nickel and other elements to form the Laves and other

intermetallics; these intermetallics are a strong sink for the austenite stabilizer, nickel. Intermetallic formation leads to nickel consumption from the austenite, and consequently to austenite destabilization and ferrite growth in SS-15Zr.

High-temperature annealing of as-cast SS-15Zr alloys leads to an increase in the $(Fe,Cr,Ni)_{23}Zr_6$ content and a corresponding decrease in the amount of austenite and Laves C15 intermetallic phases. Preliminary results of in-situ high-temperature (~1270°C) neutron diffraction studies indicate that the ferrite and Laves C36 contents of the alloy also decrease during long-term annealing [12]. Similar decreases in α-Fe and Laves phase content were observed during $Fe_{23}Zr_6$ formation in an Fe-15Zr alloy. According to the Fe-Zr phase diagram [13], $Fe_{23}Zr_6$ will replace the $ZrFe_2$ phase found in as-cast Fe-15Zr alloys under conditions of equilibrium cooling; we previously proposed a mechanism for this phenomenon [11]. A similar two-step mechanism may apply for SS-15Zr alloys:

i. $Zr(Fe,Cr,Ni)_{2+x}$ transforms into $(Fe,Cr,Ni)_{23}Zr_6$ + α-Zr

ii. α-Zr reacts with α-SS and γ-SS to form more $(Fe,Cr,Ni)_{23}Zr_6$

This mechanism accounts for the α-Zr observed within the $(Fe,Cr,Ni)_{23}Zr_6$ phase (Figs. 2a and 2b).

B. Lattice Parameters

The α-Fe phase in Fe-15Zr alloys contains mainly iron with a very small amount of dissolved zirconium; hence, the lattice parameter of this phase is very similar to that reported for pure iron [17]. The lattice parameter of the α-SS phase in SS-15Zr alloys is larger than that of α-Fe because of the many elements in the α-SS solid solution. The lattice parameters of the austenite phase (γ-SS) are typical of those found in stainless steel alloys with similar compositions [16].

The lattice parameters of both C36 and C15 Laves intermetallics in SS-15Zr alloys are smaller than the corresponding phases in Fe-15Zr alloys by ~1%. Several examples of lattice contraction and expansion in Laves intermetallics of Fe-Cr-Zr and Fe-Ni-Zr alloys have been reported in literature [18-20]. Muraoka et al. observed that nickel substitution at iron sites in $Zr(Fe_xNi_{1-x})_2$ intermetallics leads to lattice contraction [18]. Other

investigators have shown that increasing the chromium content of $Zr(Fe_xCr_{1-x})_2$ expands the intermetallic lattice [19, 20]. Since the zirconium content of Laves intermetallics in SS-15Zr and Fe-15Zr alloys is similar, the observed lattice contraction in SS-15Zr may be due to nickel substitution at iron sites. Similarly the small difference in lattice parameters between $(Fe,Cr,Ni)_{23}Zr_6$ and the corresponding phase in Fe-15Zr may be due to nickel presence at iron sites.

The Laves phases in the SS-42Zr alloy have the C14 structure. Although the chromium and zirconium content of Laves C14-1 are similar to those in Fe-10Cr-45Zr the lattice parameters are 0.3% smaller presumably because of nickel substitution at iron sites. The smaller lattice parameters of Laves C14-2 may be due to its increased nickel and smaller zirconium content. The reasons for the formation of two C14 phases in SS-42Zr are not known at this time. Laves C14-2 may be a non-equilibrium phase and may not be present after long-term high-temperature annealing of the alloy. The reasons for Laves intermetallic crystal structure differences in SS-42Zr (C14) and the SS-15Zr alloy (C36 and C15) are also not known, although a similar feature is seen in Fe-Zr alloys. Whereas stoichiometric $ZrFe_2$ has the C15 structure, iron-rich compositions in Fe-Zr alloys (Fe-15Zr alloy, for example) contain an $ZrFe_2$ intermetallic with the C36 structure [21].

Conclusions

1. The Laves polytypes in 316 stainless steel-15 wt.% Zr alloys are C36 and C15. Other phases in this alloy include the ferritic and austenitic phases of stainless steel and $(Fe,Cr,Ni)_{23}Zr_6$.

2. High-temperature annealing of 316 stainless steel-15 wt.% Zr alloys increases the volume fraction of $(Fe,Cr,Ni)_{23}Zr_6$ and decreases the amount of Laves and stainless steel phases.

3. Two Laves phases based on the C14 crystal structure but with distinctly different chemical compositions were observed in the 316 stainless steel-42 wt.% Zr alloy.

4. The lattice parameters of Laves intermetallics in both 316 stainless steel-15 wt.% Zr and Type 316 stainless steel-42 wt.% Zr alloy are smaller than the corresponding phases in Fe-Zr binary alloys. Nickel substitution at iron sites may explain the observed lattice contraction in stainless steel - zirconium alloys.

5. Although 316 stainless steel-15 wt.% Zr alloys show no elongation in uniaxial tension, they exhibit remarkable strength and ductility in compression tests.

Acknowledgments

The authors would like to thank Drs. K. Gourishankar, L. Leibowitz, and D. Hebditch for reviewing the manuscript and for helpful suggestions. The authors also acknowledge ANL's Analytical Chemistry Laboratory for chemical analyses of metal specimens. This work has benefited from the use of the Intense Pulsed Neutron Source at ANL. This facility is funded by the U.S. Department of Energy (DOE), BES-Materials Science, under Contract No. W-31-109-ENG-38. This work was also supported by the DOE, Nuclear Research and Development Program, under Contract No. W-31-109-ENG-38.

References

1. F. Laves, *Theory of Alloy Phases*, ASM, Cleveland, OH, 1956, p. 123.

2. R.L. Berry and G.V. Raynor, *Acta Crystallogr., 6* (1953) 178.

3. Y. Komura, *Acta Crystallogr., 15* (1962) 770.

4. D.J. Thoma and J.H. Perepezko, *J. Alloys Comp., 224* (1995) 330.

5. R.P. Elliot and W. Rostoker, *Trans. ASM, 50* (1958) 617.

6. D.P. Abraham, S.M. McDeavitt and J. Park, *Metall. Mater. Trans. 27A* (1996) 2151.

7. S.M. McDeavitt, J. Park and J.P. Ackerman, in B. Mishra and W.A. Avrill eds., *Actinide Processing: Methods and Materials*, TMS, Warrendale, PA, 1994, p. 305.

8. S.M. McDeavitt, D.P. Abraham, D.D. Keiser, Jr. and J. Park, *Proc. Conf. SPECTRUM '96*, Seattle, Washington, 1996, p. 2477.

9. J.D. Jorgensen, J. Faber, Jr., J.M. Carpenter, R.K. Crawford, J.R. Haumann, R.L. Hitterman, R. Kleb, G.E. Ostrowski, F.J. Rotella and T.G. Worlton, *J. Appl. Cryst. 22* (1989) 321.

10. A.C. Larson and R.B. Von Dreele, Los Alamos National Laboratory Report, *LAUR 86-748* (1986).

11. D.P. Abraham, J.W. Richardson Jr., and S.M. McDeavitt, to be published in *Scripta Metall.* (1997).

12. D.P. Abraham and J.W. Richardson Jr., Argonne National Laboratory, *unpublished research* (1997).

13. D. Arias, M.S. Granovsky, and J.P. Abriata, in H. Okamoto, ed., *Phase Diagram of Binary Iron Alloys*, ASM International, Materials Park, OH, 1993, p. 467.

14. Y. Liu, J.D. Livingston and S.M. Allen, *Metall. Mater. Trans., 23A* (1992) 3303.

15. W. Bruckner, K. Kleinstuck and G.E.R. Schulze, *phys. stat. sol., 23* (1967) 475.

16. D. Peckner and I.M. Bernstein, *Handbook of Stainless Steels*, McGraw-Hill Publishing, 1977.

17. B.D. Cullity, *Elements of X-ray Diffraction, 2nd ed.*, Addison-Wesley Publishing, 1978, p. 506.

18. Y. Muraoka, M. Shiga and Y. Nakamura, *phys. stat. sol. (a), 42* (1977) 369.

19. D. Shaltiel, I. Jacob and D. Davidov, *J. Less-Common Metals, 53* (1977) 117.

20. O. Canet, M. Latroche, F. Bourée-Vigneron and A. Percheron-Guégan, *J. Alloys Comp., 210* (1994) 129.

21. K. Kai, T. Nakamichi and M. Yamamoto, *J.Phys.Soc. Japan, 25* (1968) 1192.

List of Figure Captions

Fig. 1. Typical microstructure of as-cast SS-15Zr alloy. The dark phase is α-SS, the bright phase $Zr(Fe,Cr,Ni)_{2+x}$.

Fig. 2a. Microstructure of SS-15Zr alloy annealed for 2 h at 1275°C. The dark phase is α-SS, the bright phase is $Zr(Fe,Cr,Ni)_{2+x}$, and the gray phase is $(Fe,Cr,Ni)_{23}Zr_6$.

Fig. 2b. Microstructure of SS-15Zr alloy annealed for 2 h at 1275°C. Arrows mark some of the α-Zr phase.

Fig. 3. Microstructure of the SS-42Zr alloy showing two Laves intermetallics and the sigma phase. The matrix phase has been labeled Laves C14-1 and the triangular-gray phase as Laves C14-2 in Table 2. The sigma phase is marked by an arrow.

Fig. 4. Secondary electron image of tensile fracture surface of SS-15Zr alloy. The ferrite (white flow lines) within the eutectic structure appears to have necked to a chisel edge.

Fig. 5. Typical stress-strain behavior in compression for SS-15Zr alloy strained to failure at an extension rate of 2.2×10^{-4} cm/s.

Table 1

Typical compositions of SS-15Zr and SS-42Zr alloys (wt.%).[a]

Alloy	Fe	Cr	Ni	Zr	Mo	Mn	Si	Co	Cu	V	C
SS-15Zr	57.5	14.4	9.2	14.5	1.7	1.1	0.5	0.2	0.3	0.05	0.02
SS-42Zr	38.6	9.9	6.5	42.4	1.2	0.9	0.3	0.1	0.2	<0.05	<0.02

[a] Metal concentrations were determined by inductively coupled plasma atomic emission spectroscopy. Estimated accuracy ~ ±5%.

Table 2

Results of Neutron Diffraction and EDS measurements on various alloys

Alloy	Heat Treatment	Phases & Structure Type	Lattice Parameters (nm) (±0.0001)	Phase (vol.%)	Phase Elemental Analysis (at.%)			
					Fe	Cr	Ni	Zr
SS-15Zr	None (As Cast)	ferrite (bcc)	a = 0.2876	40 ± 5	67	25	5	<0.1
		austenite (fcc)	a = 0.3596	9 ± 1	71	19	7	<0.1
		Laves C36	a = 0.4908, c = 1.6016	33 ± 5	54	7	12	24
		Laves C15	a = 0.6938	16 ± 2	—	—	—	—
		$(Fe,Cr,Ni)_{23}Zr_6$	a = 1.1690	2 ± 1	58	10	9	20
SS-15Zr	1275°C, 2 h Furnace cooled	ferrite (bcc)	a = 0.2876	42 ± 3	68	24	5	<0.1
		austenite (fcc)	a = 0.3596	4 ± 1	71	19	7	<0.1
		Laves C36	a = 0.4909, c = 1.6018	30 ± 2	53	7	13	24
		Laves C15	a = 0.6938	13 ± 2	—	—	—	—
		$(Fe,Cr,Ni)_{23}Zr_6$	a = 1.1691	11 ± 1	58	10	9	20
SS-42Zr	None (As Cast)	Laves C14 -1	a = 0.4987, c = 0.8154	76 ± 11	47	13	7	31
		Laves C14 -2	a = 0.4975, c = 0.8126	24 ± 11	34	13	24	25
		sigma ?	—	~0.2	39	51	6	<0.1
Fe-10Cr-45Zr	1000°C, 24 h	Laves C14	a = 0.5006, c = 0.8181	>97	56	13	—	31
Fe-15Zr	1000°C, 24 h Furnace cooled	Fe (bcc)	a = 0.2867	58 ± 1	99.8	—	—	<0.2
		Laves C36	a = 0.4961, c = 1.6184	33 ± 1	75	—	—	~25
		Laves C15	a = 0.7015[a]	—	—	—	—	—
		$Fe_{23}Zr_6$	a = 1.1695	9 ± 1	80	—	—	~20

[a] Value obtained from ref. 15.

Fig. 1. Typical microstructure of as-cast SS-15Zr alloy. The dark phase is α-SS, the bright phase $Zr(Fe,Cr,Ni)_{2+x}$.

Fig. 2a. Microstructure of SS-15Zr alloy annealed for 2h at 1275°C. The dark phase is α-SS, the bright phase is $Zr(Fe,Cr,Ni)_{2+x}$, and the gray phase is $(Fe,Cr,Ni)_{23}Zr_6$.

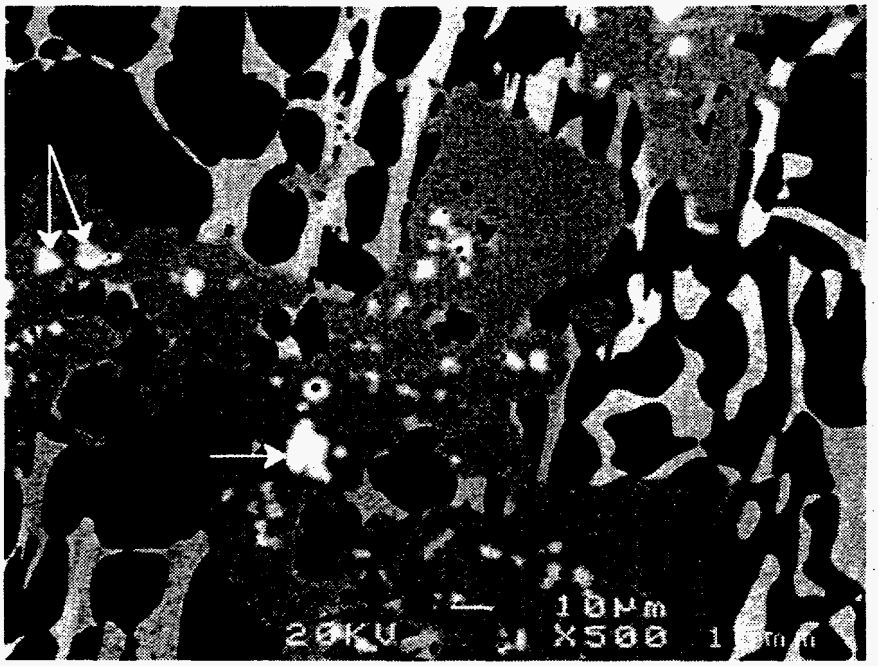

Fig. 2b. Microstructure of SS-15Zr alloy annealed for 2 h at 1275°C. Arrows mark some of the α-Zr phase.

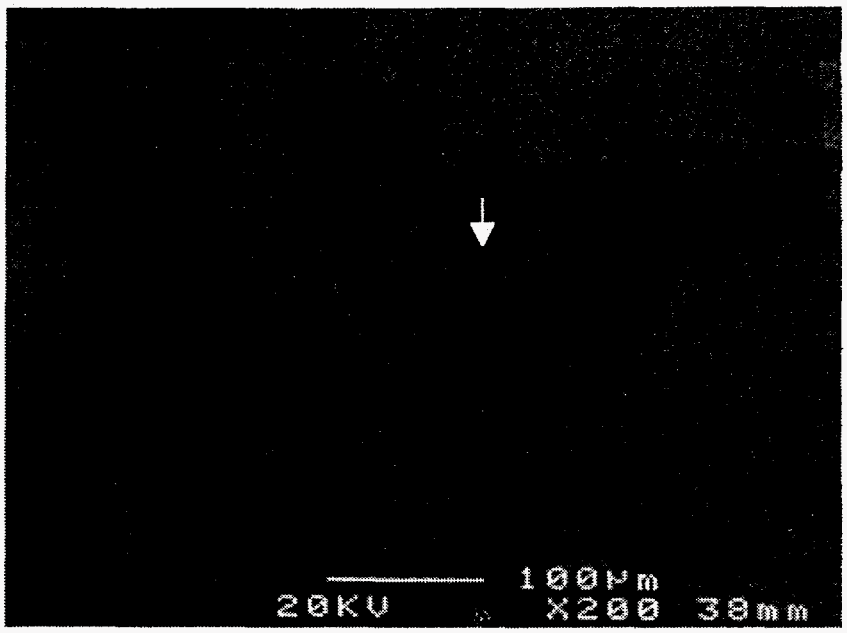

Fig. 3. Microstructure of the SS-42Zr alloy showing two Laves intermetallics and the sigma phase. The matrix phase has been labeled Laves C14-1 and the triangular-gray phase as Laves C14-2 in Table 2. The sigma phase is marked by an arrow.

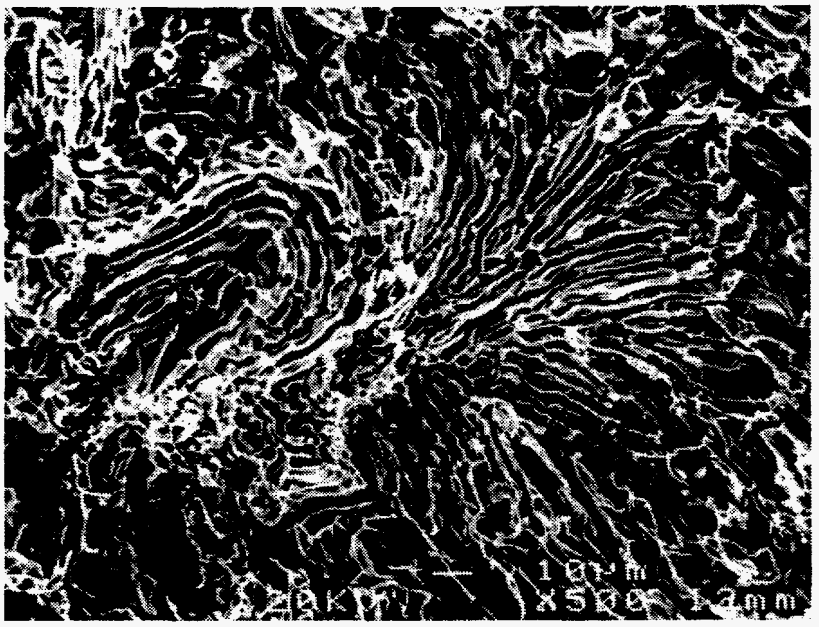

Fig. 4. Secondary electron image of tensile fracture surface of SS-15Zr alloy. The ferrite (white flow lines) within the eutectic structure appears to have necked to a chisel edge.

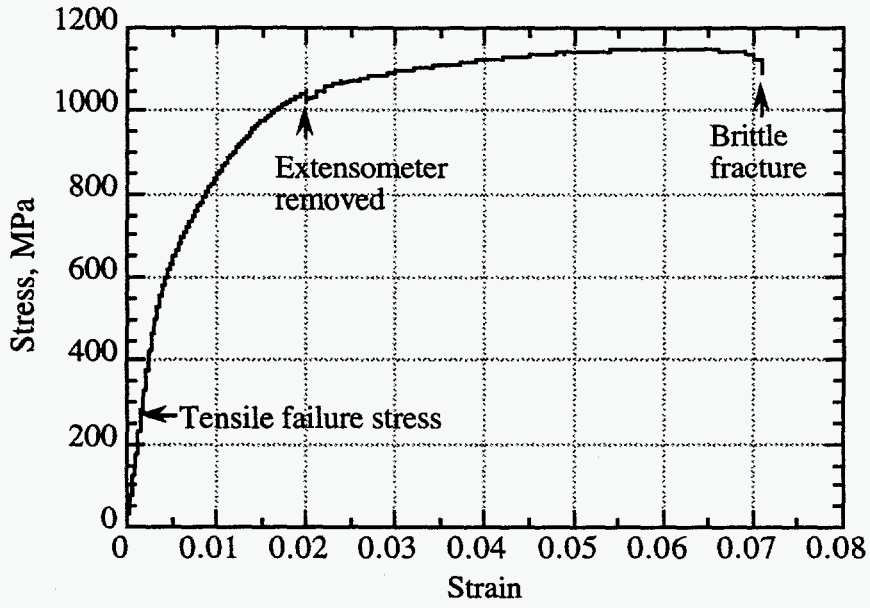

Fig. 5: Typical stress-strain behavior in compression for SS-15Zr alloy strained to failure at an extension rate of 2.2×10^{-4} cm/s.